Desorption of helium atoms from thin films

M. Sinvani and D. L. Goodstein
California Institute of Technology, Pasadena, California 91125

M. W. Cole
California Institute of Technology, Pasadena, California 91125
and Physics Department, Pennsylvania State University, University Park, Pennsylvania 16802

P. Taborek
AT&T Bell Laboratories, Murray Hill, New Jersey 07974
(Received 1 September 1983; revised manuscript received 27 April 1984)

Investigation is made of the desorption of He atoms from thin films. Three different experimental geometries are used to study the dependence on substrate material, film temperature, and duration of the heat pulse. The major conclusions are that (a) the speed distribution is similar to a Maxwellian, (b) the angular distribution is strongly focused about the normal direction, (c) desorption time constants differ systematically from estimates, and (d) a phonoatomic effect analogous to the photoelectric effect is observed. The measurements are analyzed in terms of several theoretical models. Conclusions are drawn about the time evolution of the film thickness and temperature.

I. INTRODUCTION

In spite of impressive progress in surface science, the phenomenon of desorption remains relatively poorly understood. One reason for this situation is that few systematic and detailed experimental studies have been performed, and what few there are tend to concentrate on strongly adsorbed systems. Helium, which has a binding energy substantially less than any other adsorbate, provides an ideal system to test theories of thermal desorption. Unfortunately, many of the standard techniques of surface analysis which are useful for high-temperature studies are difficult to apply in the cryogenic environment which is necessary for studying the desorption of helium.

We have adapted techniques used in previous low-temperature experiments on ballistic heat pulses to study the desorption of ^{4}He from a variety of surfaces. Small thin-film heaters and superconducting bolometers on single-crystal substrates were used to generate and detect a flux of desorbed helium atoms with very high space and time resolution. Using these devices we were able to directly observe the time evolution of the desorbed flux as well as the complete three-dimensional momentum distribution of the atoms leaving the surface. Our techniques allow us to investigate conventional thermal desorption in which the substrate is characterized by a temperature, as well as nonequilibrium desorption due to a low-power-density beam of high-frequency phonons. The ability to observe desorption due to a nonequilibrium substrate-phonon distribution gives added insight into the microscopic mechanism of desorption which is difficult to achieve using standard methods.

Most of the first-principles quantum theories of phonon-induced desorption assume that a weakly bound adsorbate such as helium should be desorbed via one-phonon processes which obey certain single-particle conservation conditions. Despite the simple and appealing nature of this idea and the close connection to the theory of inelastic atomic beam scattering, one-phonon desorption has not been observed previously in an unambiguous manner.

One of the main motivations of our work was to find a clear experimental signature of the conservation laws which govern one-phonon desorption processes. This proved to be a subtle and difficult problem because the one-phonon quantum theories often yield predictions surprisingly similar to phenomenological thermodynamic descriptions of desorption in terms of heat fluxes, thermal boundary resistance, and effective temperature. We have attempted to clarify the differences between some of the theoretical models and to use this analysis to interpret our experimental results. The data suggest that both single-phonon and multiphonon thermalization processes are important factors in desorption.

The thermal desorption of helium has been studied experimentally by a number of previous investigators.[1,2] Short reports of some of our results have been presented elsewhere.[3–8] Here we discuss this work comprehensively, summarize our interpretation of the data, and relate it to various theoretical descriptions of phonon-induced desorption. In Sec. II of this paper we describe our experimental methods. In Sec. III we present a theoretical framework based on simple models, which will guide our discussion, by separating geometrical and phase-space considerations from basic questions of mechanism. In Sec. IV we describe the experimental data and our interpretation and introduce a new differential pulse-width technique. Section V contains a summary of our results.

II. EXPERIMENTAL TECHNIQUES

In this paper we discuss experiments in which ^{4}He atoms desorbed from a film by a heat pulse are detected as

a function of their time of flight by a superconducting-transition bolometer. Three basic configurations are used. In the simplest, sketched in Fig. 1(a), an Ohmic heater forms the substrate for the He film. The bolometer is on a separate sapphire substrate, a short distance above the heater. This is called the "heater-substrate" geometry and is used, for example, in the measurements of desorption time constants. In a second geometry, depicted in Fig. 1(b), the heater is on the bottom of the crystal, and the He atoms are desorbed from the upper surface of the sapphire by phonons that have first propagated through the crystal. This is called the "crystal-substrate" geometry and is used to separate substrate-phonon from thermal desorption processes, and to separate the effects of longitudinal and transverse phonons. The third geometry, shown in Fig. 1(c), is used to measure the angular distribution of the desorbed atoms. As in the heater-substrate geometry, desorption takes place directly from the surface of a nichrome film on a sapphire substrate. In this case, however, the sapphire crystal is mounted on a vertical turntable which can be rotated by approximately $\pm 60°$. The desorption flux is detected by a bolometer fabricated on the end of a sapphire rod 2.5 mm in diameter which is mounted in a fixed vertical position. The turntable is mounted on a shaft which is supported by two sets of ball bearings. A pulley-and-belt arrangement is used to connect the turntable shaft to a similar shaft at the top of the Dewar. One set of plates of a parallel-plate capacitor is also attached to the turntable shaft; the capacitance with respect to the set of fixed plates can be measured to determine the angular position of the turntable. The heater film is precisely positioned over the stationary axis of the turntable, so as the turntable is rotated, the desorption angle changes, but the heater-detector distance does not. Both the heater- and detector-substrate crystals are mounted inside the vacuum can and are not in contact with the helium bath; they are therefore not as well thermally anchored as in the previously described geometries.

All of these experiments are made possible in part by the fact that thermal phonons propagate ballistically in sapphire crystals at low temperature.[9] This point is obvious in the crystal-substrate experiments which make direct use of ballistic phonons, but indeed all of the experiments depend on the fact that phonons are not scattered from the crystal back into the heater, so that heat pulses can be turned off as well as on very rapidly. In fact, the techniques used in these experiments have grown out of a long and systematic study of thermal phonon propagation in sapphire crystals.[9,10]

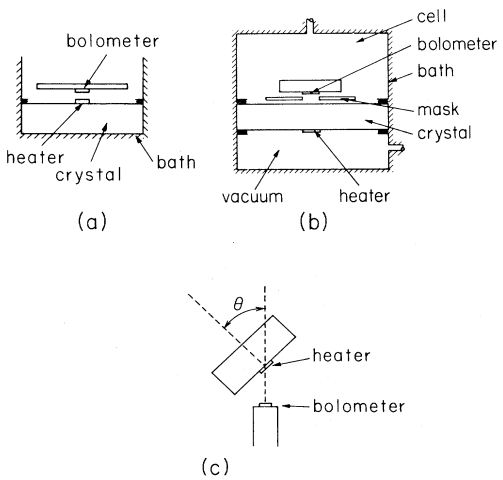

FIG. 1. Three different experimental configurations used in the present work. (a) Heater-substrate geometry, (b) crystal-substrate geometry, and (c) angular distribution geometry.

Except where otherwise noted, care has been taken to assure that experiments are performed under conditions such that the mean free path in the gas is long compared to the distance between desorbing film and bolometer. However, although the desorbed atoms do not collide with preexisting gas atoms, they may collide with each other. A simple calculation indicates that if δN atoms per unit area are desorbed in time τ, then the mean number of collisions after time t is $\sigma \delta N \ln(t/\tau)$, where σ is the cross section. Substituting numbers typical of our experiments in the heater-substrate geometry, if a full monolayer, namely $\delta N \approx 10^{15}$ cm^{-2}, is desorbed in 10^{-7} sec, with a time of flight $t \approx 10^{-6}$ sec from heater to bolometer, and we take $\sigma \approx 10^{-15}$ cm^2, then we may expect each atom to make on the order of one collision. Thus, propagation from surface to bolometer can be taken to be purely ballistic only in the crystal-substrate geometry, where the desorption fluxes are much lower.

Most elements of these experiments are conventional and need to be described only very briefly here. Novel techniques, including the use of very small, fast heaters and bolometers, and an *in situ* method that we have devised for measuring low gas pressures,[8] will be described in more detail below.

All of our experiments are performed in a cell immersed in a temperature-regulated helium bath. He gas monitored into the cell forms an adsorbed film on all exposed surfaces. Usually, a small quantity (0.165 g) of Grafoil in the cell serves as a ballast surface so that the quantity of He gas needed is not too small to manipulate in a conventional gas-handling system. The pressure in the cell, when it is high enough (above 0.1 mTorr), may be measured at room temperature by a capacitive gauge.

The sapphire crystals used in the heater-substrate and crystal-substrate experiments were flat cylinders with faces parallel to the C-X plane, and with an axis along the Y axis of the sapphire's trigonal structure. The cylinders were typically 57 mm in diameter and 9.5 mm thick (although different dimensions were sometimes used). For a crystal-substrate experiment in this case, desorption would be due to phonons propagating along the Y axis (which is not a singular focusing direction[9]). Longitudinal phonons arrive at the upper surface in about 1 μsec and transverse phonons arrived in 1.63 μsec for fast transverse (FT) [1.72 μsec for slow transverse (ST)]. Phonon dispersion is not a factor since typical heater temperatures were ~ 10 K, whereas the Debye temperature of sapphire is $\sim 10^3$ K. The substrate crystal for the heater in the angular distribution experiments was rectangular in shape ($13 \times 13 \times 6$ mm) with the large faces on which the heater film was deposited parallel to the C-X plane.

the samples were cleaned and handled with normal labo-

ratory care, but the desorption surfaces are otherwise uncharacterized. In the present stage of development of the techniques reported in this work, experimental difficulties prohibit the use of modern methods of surface preparation and analysis. This point should be kept in mind in interpreting the results presented below.

The new methods of signal analysis that we have introduced in this study require the use of small, fast heaters and bolometers which have high resolution in both space and time. Both heaters and bolometers are evaporated metallic films, where the heater is a square with 0.3-mm sides and the bolometer is in the form of a serpentine strip ~ 0.3 mm in overall dimension (i.e., ~ 0.1 mm^2 area), made by photolithographic techniques. The bolometers are 2000-Å films of Sn. The heaters are ~ 600-Å films of Constantan or nichrome impedance-matched to the 50-Ω coaxial cables that transmit pulses to them.

A pulse generator is used to provide 10-V rectangular pulses of variable width t_p ($\gtrsim 30$ nsec) to the heater. If less power is needed, an attenuator is used. The bolometer-output signal, after broadband amplification, is either displayed directly on an oscilloscope or signal-averaged using a boxcar integrator.

The bolometer is maintained at its superconducting transition at all temperatures by means of a magnetic field (produced by a superconducting Nb-wire coil outside the cell). We find that the performance (both speed and sensitivity) of the bolometer is not noticeably degraded even at temperatures as low as 1.5 K ($T_c \simeq 3.7$ K for Sn). For each measurement we choose a combination of magnetic field and bolometer bias current (typically ~ 1–2 mA) such that the bolometer signal is both stable and linear with power.

Our bolometers usually detect a relatively slowly varying signal due to a Maxwellian distribution of arriving atoms. It has been demonstrated in earlier experiments[3–8] that our bolometers have a response time of ~ 10 nsec, more than adequate for this purpose. More critical to these experiments is the response time of the heaters, which we now analyze.

Consider, as a typical case, a Constantan heater on a sapphire substrate in vacuum at temperature T_0. A step-function pulse of current causes power to be dissipated at a rate W (in watts). The temperature of the heater T_h as a function of time is determined by the conservation of energy,

$$W = C\frac{\partial T}{\partial t} + \xi(T^4 - T_0^4) , \tag{2.1}$$

where C is the heat capacity of the heater. The coefficient ξ, which may be calculated from acoustic-mismatch theory,[11,12] determines the rate at which phonons are radiated into the sapphire. In our case we find $\xi = 1.47 \times 10^{-5}$ W K^{-4}, while

$$C = (1\times 10^{-11})T + (33\times 10^{-15})T^3 \text{ W sec K}^{-1}$$

for a heater consisting of 5×10^{-8} g of Constantan. Suppose that $T_0 = 2$ K and $W = 1$ W. In steady state conditions, the heater temperature reaches

$$T_h = (W/\xi + T_0^4)^{1/4} , \tag{2.2}$$

or about 16 K. The initial temperature rise, $\partial T/\partial t \approx W/C \approx 10^{11}$ K/sec, is very rapid. As T nears T_h, the approach to steady state becomes exponential with a characteristic time constant $\tau_h = R_k C$ where R_k is the Kapitza resistance, $R_k = (4\xi T_h^3)^{-1}$. This gives $\tau_h \simeq 1\times 10^{-9}$ sec. The net result is that the heater rises to its steady-state temperature in 10 nsec or less, a time comparable to the rise time of the input pulse.

When the pulse is turned off, the initial cool-down rate is approximately $-\xi T_h^4/C$, which is, once again, about 10^{11} K/sec. The exponential decay to T_0 has a time constant $C(4\xi T_0^3)^{-1} \approx 40$ nsec, but as we shall see, at 3 K the He film has a very much longer time constant. Thus, even here the rate of change of heater temperature is practically instantaneous compared to other times in the problem.

The steady-state heater temperatures used to analyze our results are obtained using Eq. (2.2). In some cases it has been possible to cross-check these values with temperatures obtained from the times of flight of the desorbed atoms, with very good results. This point is discussed in Sec. IV.

In addition to knowing T_h, it is necessary to know the chemical potential μ of the He gas in order to estimate the thicknesses of our helium films, δ. The chemical potential is a well-known function of T_0 and P_g, the pressure in the helium gas, which must be measured. Since P_g is typically too low to be measured by most conventional means, it was originally hoped that Grafoil manometry[13] could be used. Unfortunately, we found that at low pressure the very small quantities of gas in the open parts of our cell were unduly sensitive to small departures from equilibrium in the large quantity of gas adsorbed on the Grafoil. It was therefore necessary to devise a novel means of measuring pressure.[5,8]

We observed that, in all of these experiments, the signal depended on the time between pulses, t_r, unless it was longer than some critical value, t_{rc}. The critical repetition rate t_{rc} was found to be strongly correlated with P_g, varying over many orders of magnitude when the initial thickness, δ_0, and T_0 were changed. The reason is that t_{rc} is the time needed by the film to return to its initial thickness once the heater pulse is terminated. The rate of change of film thickness is given by

$$n\frac{d\delta}{dt} = \frac{\alpha P_g}{(2\pi m k_B T_0)^{1/2}} - \dot{N}_{\text{des}} , \tag{2.3}$$

where α is the sticking coefficient and n is the number density in the film. The first term on the right-hand side of Eq. (2.3) is the rate per unit area of accumulation of atoms adsorbed from the gas. $\dot{N}_{\text{des}}$ is the rate at which atoms desorb from the film. When the heater is first turned off, the system is far from equilibrium; $\dot{N}_{\text{des}}$ is negligible compared to the first term and δ grows linearly in time at a rate proportional to P_g. Later, as equilibrium is approached, the two terms become comparable and δ approaches δ_0 exponentially. The time constant of the exponential is governed by precisely the same physics we investigate elsewhere in this paper. Using Eq. (4.4) of Sec. IV, with T_h replaced by T_0, we find values of τ which are

very short compared to the observed values of t_{rc}. Thus, except for a very brief period at the end, the film's recovery is linear in time, so that t_{rc} is proportional to P_g.[8]

We have tested these ideas in two ways. One way is by observing the signal as a function of t_r in a heater-substrate experiment. We expect the height of the bolometer signal to grow essentially linearly from zero for $t_r = t_p$, then break off sharply and become independent of t_r at a well-defined time t_{rc} which depends on P_g, but not, e.g., on heater power. Results in reasonable agreement with this expectation are shown in Fig. 2.

We have also measured t_{rc} at pressures high enough so that they could be measured directly (after appropriate correction for thermal transpiration[14]). Integrating Eq. (2.3), we then expect to find

$$t_{rc} = \frac{\Delta N}{\alpha} \frac{(2\pi m k_B T_0)^{1/2}}{P_g} , \tag{2.4}$$

where ΔN is the change in the amount adsorbed per unit area, $n\delta$, due to the heat pulse. The reuslts of the measurements are given in Table I. Over a wide range of P_g and heater power, Eq. (2.4) could be satisfied within 30% by a single choice of the parameter $\Delta N/\alpha$,

$$\Delta N/\alpha = 1\times 10^{15} \text{ atoms/cm}^2 \simeq 1 \text{ ML} , \tag{2.5}$$

where ML denotes monolayer. These measurements may be regarded as the calibration of t_{rc} as a means of measuring P_g. The uncertainty in P_g is thus about 30%, but owing to the logarithimic dependence of μ of P_g, the uncertainty in μ, the quantity of primary interest, is only about 1%. This method was used to measure μ even when P_g is as low as 10^{-9} Torr.

It would be appealing to cite our results as a function of film thickness δ_0 rather than μ. Unfortunately, the functional form $\delta_0(\mu, T)$ is not known for ^{4}He films on the sapphire or Constantan substrates in these experiments. Some guidance may be gained, however, from other surfaces for which it is known. In the case of He on Grafoil,[15,16] a plot of μ versus N shows a first-layer plateau at $-\mu = 142 k_B$, which bends over at $\delta_0 \simeq 0.6$ layers, reaching a new second-layer plateau of $-\mu = 30 k_B$ beginning at $\delta_0 \simeq 1.2$ layers. This behavior is only weakly temperature dependent. We would expect the same qualitative behavior on an ideal sapphire or Constantan surface, but at somewhat lower values of $-\mu$.[17] Thus at a given value of μ, the Grafoil data give an upper limit to the film thickness. A particularly useful fact to remember is that when $-\mu \gtrsim 30 k_B$, $\delta_0 \lesssim 1.2$ layers.

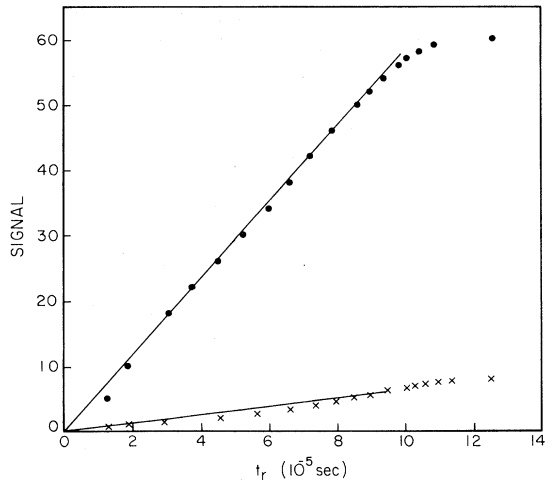

FIG. 2. Intensity of the desorption signal versus t_r for $T_h = 19$ K (●) and $T_h = 10.7$ K (×). The coverage is less than one layer. For both heater powers, $t_{rc} \approx 10^{-4}$ sec.

III. MODELS

The purpose of this section is to outline the basic possible mechanisms for desorption that one would like to be able to choose between, and to introduce a formalism for analyzing the results of flash-desorption experiments. We shall see that the signal observed in these experiments depends in rather complicated ways on the geometry and other parameters of the experiment, but conversely, tht quite different mechanisms of desorption lead to rather similar signals. We first discuss various models of desorption, then compute desorption rates for later comparison to data from two simple models that may be considered extreme limiting cases. We then introduce the formalism by means of which desorption rates may be

TABLE I. Values (Ref. 8) of t_{rc} for different coverages N [given in cm^3 (STP) of gas] and T_0. The pressures $P_g(t_{rc})$ calculated using Eqs. (2.4) and (2.5) are given in comparison with the measured pressures P_g. The values of μ in the last column were calculated from $P_g(t_{rc})$.

N [cm^3 (STP)]	T_0 (K)	$10^4 t_{rc}$ (sec)	$P_g(t_{rc})$ (mTorr)	P_g (mTorr)	μ (K)
0.499	3.8	12.5	0.1	0.13	67
0.675	3.8	1.67	0.7	0.6	59
0.675	3.483	9.76	0.12	0.13	60
0.817	3.48	0.12	9.4	7.4	44.6
0.817	3.39	0.2	5.6	5.3	45
0.817	3.23	0.51	2.1	2.9	45.6
0.817	2.978	1.34	0.8	1.0	44.5
0.817	2.644	10.2	0.1	0.14	44.2

translated into detector signals, and finally, discuss the effects of geometry using one of the models as an example. We do not, in this section, consider the further complications introduced by possible collisions between desorbing gas atoms.

A. Models of desorption

Microscopic models of desorption generally assume that the substrate-phonon bath interacts with isolated adsorbed atoms.[18–30] The simplest further assumption is that single phonons of sufficient energy lead to desorption of an atom while conserving the total energy and the component of momentum parallel to the surface. Even in this simple model, there is not general agreement over the nature of the phonon-atom interaction.[31]

One may also consider processes in which an atom is first excited by an incident phonon or phonons, then desorbed by a subsequent one. The states into which the atoms are excited are the bound states of the atom in the attractive well due to the substrate. These may be the states of a single atom on the substrate, or they may be modified by the presence of other adsorbed atoms. In these cases, rates are important because atoms may deexcite by radiating phonons before they can be desorbed.

A new level of complexity is introduced if one permits the substrate phonons to interact with states of the film representing motions parallel to the substrate. The film can be thought of as having a temperature of its own, loosely coupled to the phonons of the substrate. In the extreme model of this kind,[32,33] the film is treated as a continuum thermodynamic system, with desorption occurring because the film is warmed, thereby raising its vapor pressure.

As we shall see in more detail below, all of these models tend to predict rather similar Maxwellian distributions of desorbed atoms from a thermally pulsed substrate. In the case of the thermodynamic model, the Maxwellian arises because the desorption rate is deduced from considerations of detailed balance with the adsorbate vapor. On the other hand, single-phonon models produce Maxwellians because only the Boltzmann tail of substrate phonons with energy greater than the binding energy of the adsorbate can cause desorption.

B. Two examples

We consider explicitly two representative models for comparison to data. One is the simple detailed-balance (SDB) picture, of which the thermodynamic continuum model mentioned above is a special case. The other, which we denote SPCME (single-phonon constant matrix element), is a simple example of a microscopic model.

In the SDB model the velocity distribution of desorbing atoms is deduced by applying detailed balance to the inverse process of sticking from the vapor. In other words, we assume the film is in a state that could be in equilibrium with a vapor, even though it is not. We further assume that an atom incident from the vapor can suffer only two possible fates: sticking, with probability α, or elastic, specular reflection with probability $1-\alpha$.

With these assumptions, the number of atoms per unit time and area desorbed into solid angle $d\Omega$ and about Ω is given by the sticking coefficient multiplied by the incident rate,

$$dJ(\Omega,E)=(\beta^3/2\pi^3 m)^{1/2} n\alpha E\cos\theta\exp(-\beta E)dE\,d\Omega\ , \tag{3.1}$$

where E is the kinetic energy and m the mass of the desorbed atom, θ is the angle with respect to the surface normal, and

$$n=\lambda^{-3}\exp(\beta\mu)\ ,$$

where $\lambda=\hbar(2\pi\beta/m)^{1/2}$, and $T=(k_B\beta)^{-1}$ is the film temperature.

The second model that we consider is based on a microscopic quantum-mechanical description of the desorption process. The first simple one-dimensional quantum calculations of phonon-induced desorption were formulated as early as 1935;[18] since then the subject has received considerable theoretical attention[19–30] and has become much more sophisticated. The basic idea of these theories is that surface atoms of a substrate are displaced from their equilibrium positions when a phonon is reflected from the interface. This, in turn, causes a time-varying force on the adsorbed atoms which can perturb them sufficiently to cause desorption. The Hamiltonian which describes the phonon-adatom interaction can be approximated as $H=-\vec{u}\cdot\vec{\nabla}V$ where $\vec{u}$ is the surface displacement and V is the adatom-surface potential. The desorption rate is proportional to the squared matrix element of the Hamiltonian. A perturbation-theory calculation can yield the total desorption rate as well as the dependence on atomic energy and angle. Although the detailed results depend on the exact form of the interaction potential V, several qualitative conclusions have emerged from the model calculations. (1) If the adatom binding energy is less than the Debye temperature of the substrate (as is the case in all of our experiments), then desorption is expected to take place via absorption of a single phonon or a sequence of one-phonon transitions through excited states; multiphonon effects are not important. (2) The desorption rate has the Arrhenius form with $\tau\propto e^{Q/T}$. (3) The desorption flux is not isotropic. Atoms are ejected preferentially in the direction normal to the substrate surface.[22–24] (4) Atoms which do emerge at larger angles have a lower average kinetic energy.[22]

Rather than adopt any one of the proposed models, we have formulated a simplified model which retains many of the physically significant features of the detailed calculations. In particular, we assume that the helium-substrate potential is translation-invariant (many of the published calculations assume a highly corrugated potential with localized adsorption sites), and that desorption takes place in a one-step process in which one phonon of energy $\hbar\omega$ desorbs one atom. These assumptions imply that both the energy and parallel momentum of the single particles involved in the process are conserved. We also assume that the cross section for interaction is independent of the initial or final states of the atom, but depends only on the square of the amplitude of the phonon displacement, which is proportional to ω^{-1}. Because of the

single-phonon and constant-matrix-element assumptions, we call this the SPCME model. The desorption rate per unit solid angle, time, energy, and area is given by

$$J(\Omega,E)\propto\int_{\omega>cK_{\parallel}} d^3K\cos\theta\frac{f(\omega)}{\omega}\delta(\hbar\omega-E-E_b)\times\delta(\vec{\mathbf{K}}_{\parallel}-\vec{\mathbf{p}}_{\parallel}) , \tag{3.2a}$$

where $\vec{\mathbf{p}}_{\parallel}$ is the parallel component of momentum of the desorbed atom, $\vec{\mathbf{K}}$ is the wave vector of the incident phonon and $\vec{\mathbf{K}}_{\parallel}$ is its surface component, E_b is the adsorbed atom's binding energy, c is the phonon phase velocity, and $f(\omega)$ is the Bose distribution function, $f(\omega)=(e^{\beta\hbar\omega}-1)^{-1}$.

In this model only phonons with energy $\hbar\omega>E_b$ can cause desorption, so $f(\omega)\sim e^{-\beta\hbar\omega}$. The energy δ function in Eq. (3.2a) then has the effect of extracting the factor $e^{-\beta E}$ from the integral, which leads to the same Maxwellian character as Eq. (3.1). The parallel-momentum δ function, as well as the inequality which defines the region of integration, govern the angular distribution of the flux. These two conditions are the basis of the highly anisotropic flux distributions obtained in one-phonon-type models as discussed further in Sec. IV C.

With the use of the approximation $f(\omega)=e^{-\beta\hbar\omega}$, the integral in Eq. (3.2a) can be carried out to yield

$$J(\Omega,E)\begin{cases}\propto E^{3/2}\dfrac{\exp[-(E+E_b)\beta]}{E+E_b}\cos\theta & \text{if } E+E_b>cp_{\parallel} ,\\ =0 & \text{otherwise.}\end{cases} \tag{3.2b}$$

C. Formalism for analyzing the signal

Regardless of the mechanism of desorption, the bolometer signal $S(t)$ depends, in principle, on desorption events occurring at all previous times and at all points on the desorbing surface. Let the contribution of particles desorbing in unit time about $t'=0$ to the rate of arrival at the detector be $\dot{N}_0(t,0)$. Then,

$$\dot{N}_0(t,0)=\int_{A_s} d^2r\int' dJ(\Omega,E)\delta(t-l/v_z) , \tag{3.3}$$

where v_z is the normal component of velocity, $v_z=(2E/m)^{1/2}\cos\theta$, l is the separation between the parallel planes of desorption and detection, A_s is the emitting area, and the prime over the integral indicates that only trajectories striking the detector are included. Neglecting collisions, the total arrival rate at the detector is given by

$$\dot{N}(t)=\int_{-\infty}^{t} dt'\dot{N}_0(t-t',t') . \tag{3.4}$$

This general expression incorporates, in principle, the time evolution of the film. If the desorbing velocity distribution is time independent, the only relevant argument of $\dot{N}_0$ is $t-t'$, the time of flight.

We may express the detected signal $S(t)$ in terms of an analogous function $S_0(t,0)$ the signal arising only from desorption in unit time about zero,

$$S(t)=\int_{-\infty}^{t} dt'S_0(t-t',t') . \tag{3.5}$$

The implicit assumption here is that the detector is linear. For the case of superconducting thin-film bolometers, this is satisfied[34] for input varying slowly during a thermal relaxation time (of order 10 nsec here). In this regime the signal is proportional to the energy flux delivered to the detector,

$$S_0(t,0)=K\langle\alpha E_d(t)\rangle\dot{N}_0(t,0) . \tag{3.6}$$

Here, K is the bolometer sensitivity, α is the sticking probability for particles incident on the bolometer, and E_d is the heat deposited by a sticking atom. For constant α, this can be shown (Appendix A) to satisfy

$$E_d=E+q_{\rm st}-5/2\beta\equiv L+E , \tag{3.7}$$

where $q_{\rm st}$ is the isosteric heat of desorption of the film on the bolometer.

D. Geometric effects

To illustrate the effects of heater and detector geometry, we apply our formalism explicitly to the SDB model. Substituting Eq. (3.1) into (3.3) gives

$$\dot{N}_0(t)=(v_z^3/l)n\alpha(m\beta/2\pi)^{3/2}\exp(-\beta E_z)I_N , \tag{3.8}$$

$$I_N=\int_{A_s} d^2r\int'\exp[-\beta(E_x+E_y)]dv_xdv_y , \tag{3.9}$$

with $v_z=l/t$ and $E_i=mv_i^2/2$. Similarly, the signal is obtained from the integrated number, multiplied by sticking coefficient and energy,

$$S_0(t,0)=K(v_z^3/l)n\alpha^2(m\beta/2\pi)^{3/2}\exp(-\beta E_z)I_S , \tag{3.10}$$

$$I_S=\int_{A_s} d^2r\int'\exp[-\beta(E_x+E_y)](E+L)dv_xdv_y . \tag{3.11}$$

Here, the effects of geometry have been subsumed in the integrals I_N and I_S. Calculations of I_N and I_S in various geometries are presented in Appendix B.

Let us summarize some salient results for a plane-parallel heater and detector. For a point source, and a detector that is either very small or very large,

$$\frac{S_0(t,0)}{\max(S_0)}=t_r^{-n}[1-x(1-t_r^{-2})]\exp[(x+n/2)(1-t_r^{-2})] , \tag{3.12}$$

$$t_r=t/t_m , \tag{3.13}$$

$$x^{-1}=1+\gamma t^2m , \tag{3.14}$$

where t_m is the position of the maximum. For a small detector, $n=5$ and $\gamma=2L/ml^2$. For a large detector, $n=3$ and $\gamma=2(L+\beta^{-1})/ml^2$.

The basic behavior here is that

$$S_0(t,0)\propto t^{-n}e^{-\beta ml^2/2t^2}(E_z+L) , \tag{3.15}$$

with the power n changing from 5 for a small detector to 3 for a large one.

Operationally, one often wishes to find the temperature of the desorbing gas from the position of the signal maximum. This is easily done if n is known. Differentiating (3.12) yields

$$\beta=(2t_m^2/ml^2)(n/2+x) . \tag{3.16}$$

If the source and detector are small but finite squares with sides $2b$, and $2a$, respectively, we find

$$I_N \approx \left[4b^2+\frac{a^2v_z^2}{l^2}\right]\exp\left[-\beta\frac{mv_z^2}{2l^2}\left[\frac{2a^2}{3}+\frac{4b^2}{2\pi}\right]\right].$$

This has the effect of replacing l by an effective weighted average l_{eff}, where

$$l_{\text{eff}}^2=l^2+2a^2/3+2b^2/\pi\ .$$

Finally, if the source is infinite but the detector is small, we find a result of the form (3.16) with $n=3$. That is the same as the result in the opposite limiting case of small source and large detector.

IV. EXPERIMENTAL DATA AND INTERPRETATION

A. Signal shape

We begin this section by analyzing the bolometer signal due to pulsed desorption in light of the results of Sec. III. Our purpose here is twofold. First, we wish to determine whether the signal shape provides a means for discriminating between models of the kind we have considered. Second, we seek a dependable empirical formula for the signal shape for use in analyzing experiments.

To help sort out the many factors that can influence a bolometer signal $S(t)$, we consider the results of an experiment in which desorption from a heater is detected by a bolometer directly opposite and parallel to it. The heater and bolometer each have an area ~ 0.1 mm^2 and are separated by 1.25 mm ($A_s \ll l^2$) which allows us to use the small source and detector expression, Eq. (3.12). The pulse width, $t_p=30$ nsec, is much less than the characteristic times of flight, $t\simeq 3$ μsec, in the experiment. As we shall see later, the experimental results indicate that desorption proceeds primarily at constant temperature, permitting us to write [using Eq. (3.5)],

$$S(t)=\int_0^{t_p} S_0(t-t',t')dt'$$

$$\cong t_p S_0(t)\ .$$

With these simplifications it is easy to predict $S(t)$ for various models.

Figure 3 shows a typical desorption signal as observed experimentally (the solid line), compared to the results of the two models we discussed in Sec. III. The two formulas that fit the curve are

$$S(t)=C_1 t^{-5}\left[\frac{m}{2}\left[\frac{l}{t}\right]^2+L\right]\exp\left[-\beta\frac{m}{2}\left[\frac{l}{t}\right]^2\right] \tag{4.1}$$

for the SDB model [Eq. (3.15)], and

$$S(t)=C_2 t^{-5}\exp\left[-\beta\frac{m}{2}\left[\frac{l}{t}\right]^2\right] \tag{4.2}$$

for the SPCME model [Eq. (3.2b)]. In each case the temperature and scale factor are chosen to fit the position and magnitude of the signal maximum. Although either model thus leads to a reasonable representation of the shape of the curve as one can see from Fig. 3, we will see that the two lead to different conclusions about the temperature of the desorbing atom.

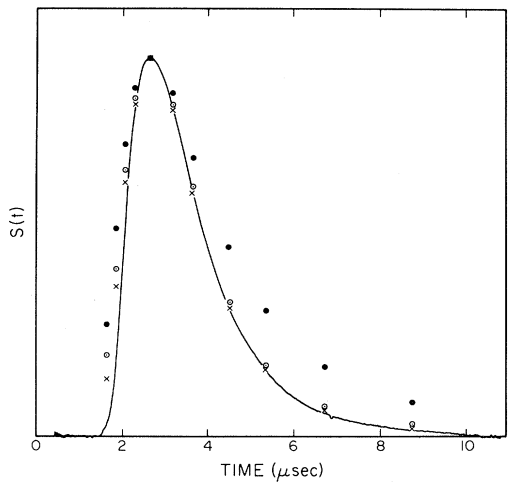

FIG. 3. Signal $S(t)$ measured for $T_h=19$ K (solid line) compared to the prediction of the SDB model, Eq. (4.1) ($\times$), and the SPCME model, Eq. (4.2) ($\triangle$). For comparison we show ($\bullet$), Eq. (4.1) with t^{-5} replaced with t^{-3} (SDB model for infinite source). The models are normalized to agree with the maximum.

Figure 4 shows a series of signals in which, under otherwise identical conditions, we have varied the heater power, and hence the heater temperature. It is seen that the higher the pulse power, the shorter the time to the signal maximum. One would like to use the time of the signal maximum as a thermometer for measuring the temperature of the desorbing atoms.

Equation (3.16) gives β in terms of t_m, the time of the signal maximum for the SDB model. For the SPCME model the dependence is also given by Eq. (3.16), but with $x=0$.

In Fig. 5 we show, as a function of heater power, the temperature deduced from the SDB and SPCME models

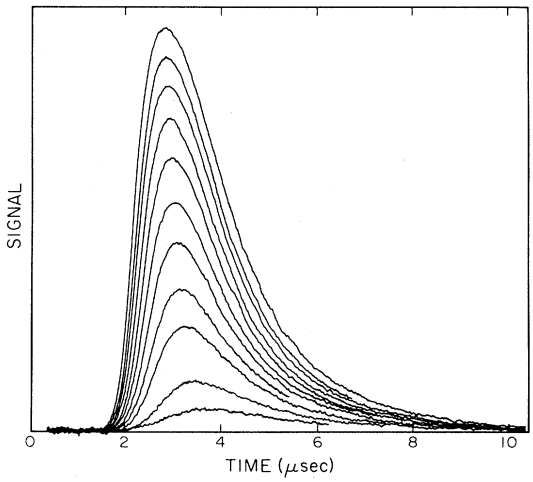

FIG. 4. Signal for various heater temperatures. In ascending order, $T_h=10.1$, 10.7, 12.0, 12.7, 13.4, 14.2, 15.1, 16.0, 16.9, 17.9, and 19 K. The chemical potential $\mu=64$ K. The pulse width is 30 nsec.

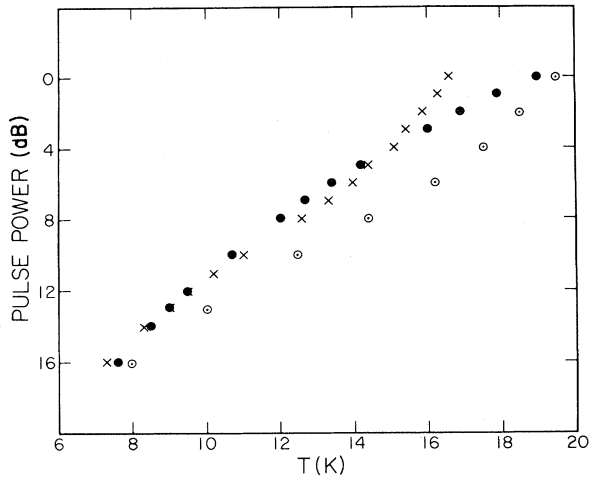

FIG. 5. Desorbed atoms' temperature as calculated from Fig. 4 peak arrival times using the SDB model (×) or SPCME model (⊙). The solid circles represent the heater temperature calculated from the acoustic-mismatch model, Eq. (2.2).

for the measured values of t_m at different heater powers, and also the heater temperature T_h according to Eq. (2.2). The two models disagree with each other, by 10—20 % in temperature, with the SDB model, in better agreement with T_h. The SDB model disagrees with T_h above 15 K, but this is to be expected. As we shall see below, desorption takes place in a time τ which depends on the film temperature. Above 15 K, τ becomes so short that desorption occurs before the heater reaches T_h, so the time-of-flight temperature cannot be expected to agree with that value.

As a further test of our formulas for $S(t)$, in Fig. 3 we have also plotted the best curve given by Eq. (4.1), but with the factor t^{-5} replaced by t^{-3}. This form would result if either the source or the detector were large rather than small in the SDB model (see Sec. III). It would also result if the sticking coefficient α, rather than being constant, was proportional to v_z^{-1} (a form suggested by earlier investigators[1]). Figure 3 makes it clear that this formula does not give an adequate representation of the data.

These comparisons may be taken as empirical evidence that the times of flight of the desorbing atoms (interpreted according to either of the models we have presented) is a reasonably dependable thermometer for the surface temperature. Any collisions that may occur among desorbing atoms do not appear to have a substantial effect on $S(t)$.

Some further comments are in order about the signal shape. In most of the experiments reported in this paper, care has been taken that the mean free path in the preexisting gas be long compared to the propagation distance l. This is easily achieved for films of the order of 1 ML. Slightly thicker films are studied by lowering the ambient temperature. In the opposite limiting case, with a mean free path short compared to l, one observes sound in the gas. The sound signal is much narrower than the ballistic $S(t)$ and arrives at much later times. It is also symmetric, a positive signal followed by a negative one. In some cases, we have filled the cell with superfluid helium and

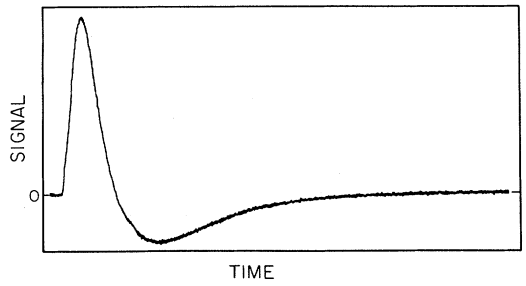

FIG. 6. Signal seen at high ambient pressure such that desorbed atoms do not propagate ballistically.

observed a second-sound signal.[4]

In the intermediate case between ballistic and hydrodynamic, or sound, propagation, the signal $S(t)$ begins to develop an undershoot at long times, as shown in Fig. 6. At still higher pressures, the undershoot is enhanced and the signal begins moving to later times, developing smoothly into the characteristic sound signal. As a practical matter, the undershoot is a valuable indicator that collisions with preexisting gas have begun to occur, and conversely, its absence assures that they have not.

As we have seen earlier, however, we do expect collisions between desorbing atoms. On the order of one collision per atom is expected in high-temperature heater-substrate experiments. The evidence presented in this section indicates that whatever the effects of these collisions, the formulas for $S(t)$ arising out of our simple models do give an accurate empirical account of the data, and afford a dependable means of measuring the temperature associated with the desorption flux.

B. Desorption time constant τ

Figure 7 shows a series of spectra made in the same heater-substrate geometry as those in Fig. 4. For the spectra in Fig. 7, however, the heater power has been kept

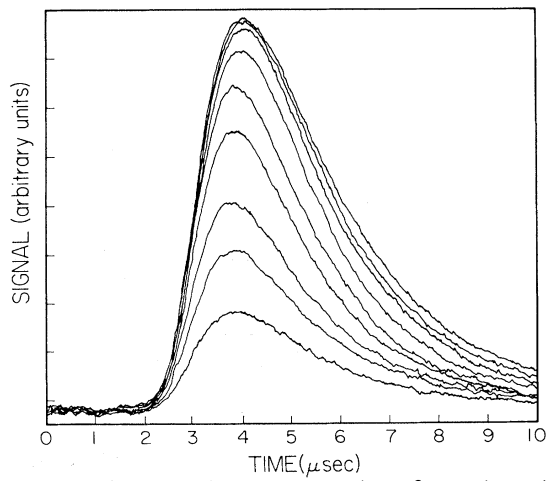

FIG. 7. Bolometer signal versus time for pulse widths t_p=0.03, 0.06, 0.08, 0.15, 0.22, 0.5, 1, 1.5, and 2.5 μsec, in ascending order. T_h=8.2 K, ambient T=3.48 K, and the chemical potential is 72 K. Heater-substrate geometry is used.

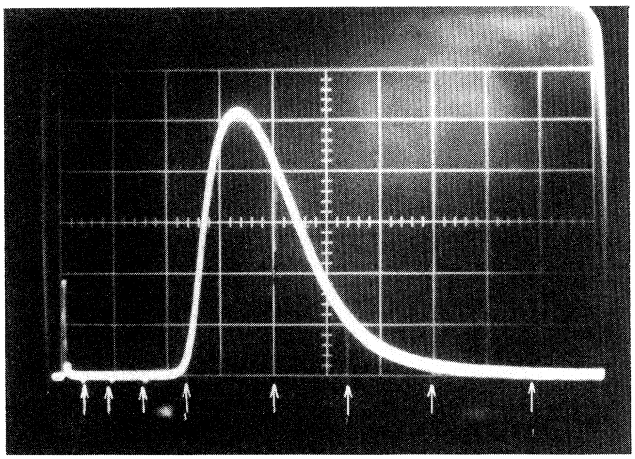

FIG. 8. Desorption signal for different values of pulse width $0.2 < t_p < 9$ μsec. The arrows indicate the ends of the pulses. Shown are eight saturated signals for different pulse widths, exposed on the same camera film.

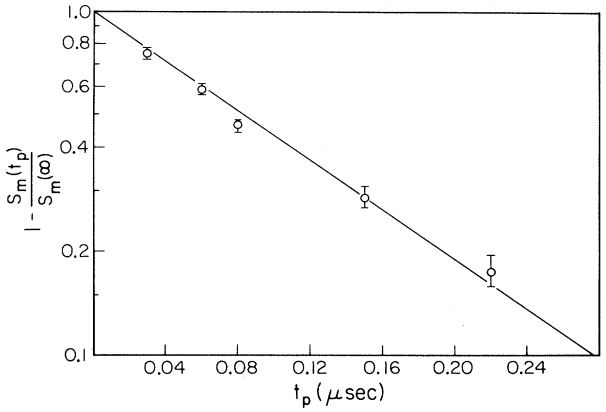

FIG. 9. Dependence of signal maximum on pulse width for data of Fig. 7. Straight line gives $\tau = 0.11$ μsec.

constant, while the pulse width t_p was varied. A proper analysis of these data requires deconvoluting the integral in Eq. (3.4). There is, however, a *qualitative* trend in the data which may be understood without further analysis. As t_p increases from ~ 30 nsec to ~ 0.5 μsec, the signal increases, but it saturates thereafter, showing no appreciable change for longer pulses. We interpret this observation to mean that the film adsorbed on the heater has reached steady state after ~ 0.5 μsec, so that keeping the heater on for longer times has little effect on the signal. This observation of saturation of the signal as a function of t_p makes it possible for the first time to directly measure the characteristic time τ for a film to reach steady state on a heated substrate. The saturation effect is emphasized in Fig. 8, where, for a film of initially ~ 1.2 ML and $T_h = 11$ K, we find no change in the signal as t_p goes from 0.2 to 9 μsec, a time much longer than the times of flight in the experiment.

Upon first reporting this phenomenon, we extracted quantitative values for τ from our data by observing that the height of the signal maximum as a function of t_p, $S_{\max}(t_p)$, approached its saturation value exponentially,[15]

$$S_{\max}(t_p) \sim 1 - e^{-t_p/\tau} , \tag{4.3}$$

corresponding to an exponential decay of the film with time constant τ (see Fig. 9). For each set of initial conditions (film μ and ambient temperature), a value of τ was thus found by measuring $S_{\max}(t_p)$ for varying t_p at constant heater power, and hence a constant heater temperature T_h.

With the same initial conditions, the procedure was repeated at different heater powers, thus generating data for the dependence of τ on T_h. Plots of $\ln\tau$ versus T_h^{-1} were found to be excellent straight lines, indicating a functional dependence of the form

$$\tau = \tau_0 e^{E_0/k_B T_h} , \tag{4.4}$$

where τ_0 and E_0 are empirical parameters having the dimensions of time and energy, respectively. Examples of such behavior appear in Fig. 10.

Equation (4.4) is alternatively referred to as the Arrhenius, or Frenkel, formula. This activated dependence on temperature is a common prediction of theories of desorption,[18–29] which are in wide disagreement, however, on the interpretation of τ_0 and E_0. A previous indirect attempt to measure τ by signal deconvolution was made by Cohen and King.[1] Cohen and King studied one of the same systems we are dealing with here, namely ^{4}He desorbed from Constantan wire, and concluded that E_0 was the film chemical potential and $\tau_0 = 2\times 10^{-7}$ sec. As we shall see, quite different results have been obtained in the present study.

To study the dependences of E_0 and τ_0, we repeated the procedure described above for various initial temperatures T_0 and amounts of helium in the cell, N_0.[5] The film thickness on the heater is not easily related to N_0 since the vast majority of the adsorbing surface area in the cell resides in the Grafoil ballast, but for each experiment the chemical potential was measured by the critical–repetition-rate technique described in Sec. II. The results of these measurements are shown in Table II and Fig. 11.

Examination of Table II shows that τ_0 is always much shorter than the value inferred by Cohen and King, being in the range 10^{-9} to 10^{-10} sec. As seen in Fig. 12, E_0 is strongly correlated with μ, given roughly by $E_0 \simeq \frac{2}{3}|\mu|$.

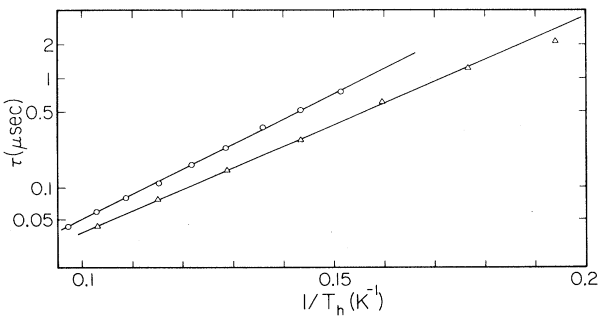

FIG. 10. Plots of τ vs $1/T_h$. Data shown are for two distinct coverages, given in fifth (upper) and sixth (lower) rows of Table II.

TABLE II. Summary of data for nichrome and Constantan (*) heaters. First two columns give the temperature and chemical potential of the film before the heat pulse. Third and fourth columns give parameters in Eq. (4.4) for each set of initial conditions.

T (K)	$-\mu$ (K)	E_0 (K)	$10^{10}-\tau_0$ (sec)
3.75	94	60±4	2
3.50	94	65±2	1
3.48	94	62±2	1.3
3.48	84	56±2	1.6
3.48	80	54±2	2.7
3.48	72	45±2	5
3.27	64	33±2	13
2.71	61	32±2	13
1.50	30	20±2	15
3.49	94*	59±2*	4*
3.8	56*	43±4*	2*

In addition, τ_0 varies with E_0, as seen in Fig. 11. This dependence is known as the compensation effect.[29]

The theoretical significance of the magnitude of τ_0, and of the relation between E_0 and μ is unclear. However, the data summarized in Table II make it possible to estimate the time constant τ over a variety of film thicknesses and heater temperatures. Because of the exponential form of Eq. (4.4), the resulting values of τ will range over many orders of magnitude.

The interpretation of these time-constant results is one of the central concerns of our study. Broadly speaking, the questions raised are of two types. In the first we ask why exponential behavior is observed. In the second we seek an explanation for the particular value of τ. The latter topic will be discussed in the following section.

To answer the first question, we have invented a method of data analysis which we call the differential—pulse-width (DPW) technique. As its name implies, it is used by comparing data obtained with slightly different pulse widths. Perhaps, surprisingly, it accomplishes the desired goal of deconvoluting the data. To be specific, the DPW method yields the time dependence of *both* the desorption rate $D(t)$ and the velocity distribution.

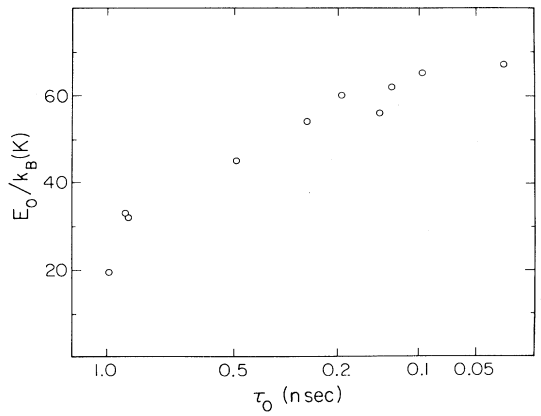

FIG. 11. Parameters τ_0 and E_0 fitted to the τ data, according to Eq. (4.4). See Table II for film conditions.

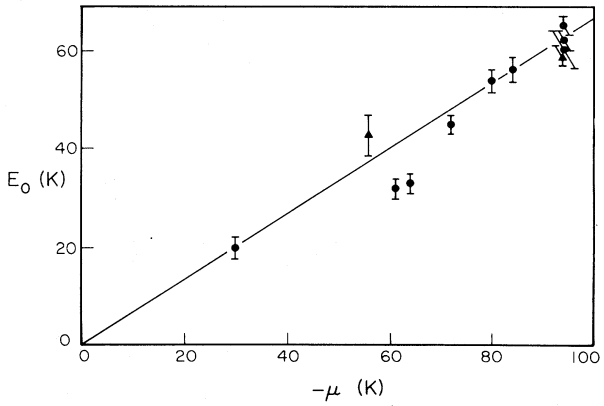

FIG. 12. Film chemical-potential dependence of the activation energy E_0 appropriate to the time-constant expression (4.4) obtained from semilogarithmic fits such as in Fig. 10. Solid line is $2|\mu|/3$. Data shown are for nichrome (●) and Constantan (▲) heaters.

The DPW method is derived from Eq. (3.5), which we may rewrite without loss of generality as

$$S(t;t_p)=\int_0^{t_p} dt' D(t') G(t,t') , \tag{4.5}$$

where G is the signal at time t per particle desorbed at time t'. Differentiating with respect to pulse width,

$$\frac{\partial S(t;t_p)}{\partial t_p} = D(t_p) G(t,t_p) . \tag{4.6}$$

This means that the signal at time t changes with pulse width ($t_p \rightarrow t_p + \delta t_p$) by an amount equal to the product of the differential number of atoms desorbed, $D(t_p)\delta t_p$, with $G(t,t_p)$. Thus the deconvolution process is accomplished by computing differences in signals. As in any difference technique, stability and lack of drift of the apparatus is important. We exemplify this method by presenting in Fig. 13 the finite-difference version of the derivative given

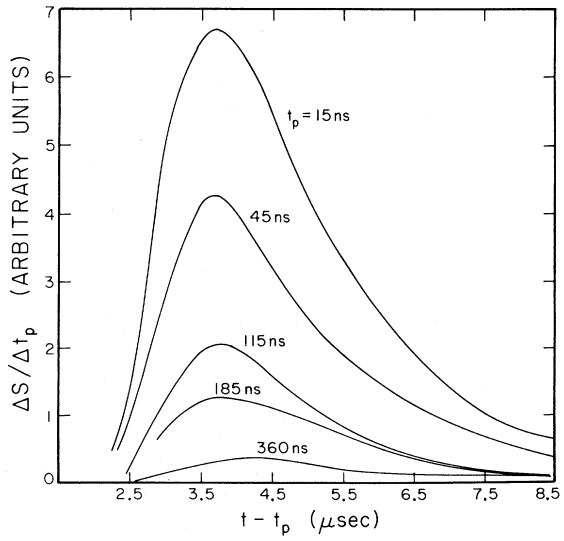

FIG. 13. Distribution of times of flight of atoms desorbed at various times after heat pulse begins, obtained by finite-difference DPW analysis of data in Fig. 7.

in Eq. (4.6). Note that the abscissa is $t-t_p$. This lets us test the tentative hypothesis that G depends only on the difference between its two arguments (the launch and detection times), indicating constant desorbed-atom temperature. Insofar as the shape of the curves in Fig. 13 is common, the hypothesis is confirmed. Moreover, the result shows that the desorbed atoms reach their final temperature almost immediately.

The time dependence of the desorption rate $D(t)$ may be separated out of Eq. (4.6) by the following argument. We integrate Eq. (4.6) over t,

$$\int dt \frac{\partial S}{\partial t_p} = D(t_p) \int dt\, G(t,t_p)$$

$$= \langle S \rangle D(t_p) , \tag{4.7}$$

where $\langle S \rangle$ is proportional to the mean signal due to a particle emitted at t_p. If the signal is either independent of the particle's kinetic energy or if the emitted particles' velocity distribution is constant in time, $\langle S \rangle$ is a constant. Supposing this to be true, it means that the desorption rate is proportional to the left-hand side of Eq. (4.7), i.e., the area under an appropriate curve of Fig. 13.

Alternatively, we evaluate the maximum of the right-hand side of Eq. (4.6) as a function of t,

$$\max\left[\frac{\partial S}{\partial t_p}\right] = D(t_p)\max[G(t,t_p)]$$

$$\equiv G_m D(t_p) . \tag{4.8}$$

Again, G_m is a constant if the film temperature (i.e., desorbed $\vec{v}$ distribution) is independent of time. In this case, Eq. (4.8) means that the desorption rate at time t_p is proportional to the maximum of the appropriate differential curve. We have applied this latter technique to determine the function $D(t)$ shown in Fig. 14. The results are seen to be in reasonably good agreement with an exponential dependence. The time constant 0.12 μsec agrees with the value (0.11 μsec) obtained by using Eq. (4.3), which treats only the peak maxima.

This differential method thus yields all the information available in the signal, obviating a model-dependent deconvolution analysis. In Fig. 13 we see the evolution of the signal coming from atoms desorbed at well-defined times after initiation of the pulse. One may thereby track the detailed evolution of both the film temperature and desorption rate.

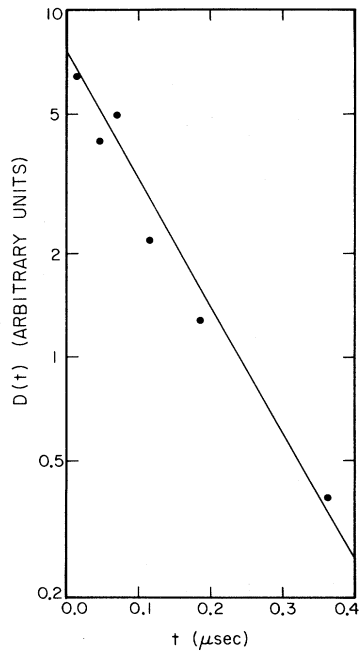

FIG. 14. Desorption rate obtained from the maxima of curves in Fig. 13 plotted semilogarithmically as a function of time. The straight line corresponds to $\tau = 0.12$ μsec.

C. Angular distribution of desorption and the critical cone

The angular distribution of the desorbed atoms is one of the few characteristics of desorption for which the two models described in Sec. III provide radically different predictions. The SDB model predicts a $\cos\theta$ distribution, while the angular distributions in the SPCME model is determined by the parallel-momentum distribution of the incident phonons and the kinematic conservation conditions. The fact that the momentum of a phonon of a given energy is more than an order of magnitude less than the momentum of a free atom of the same energy leads to some spectacular effects in the angular distribution which can be illustrated by a simple diagram. Figure 15 shows

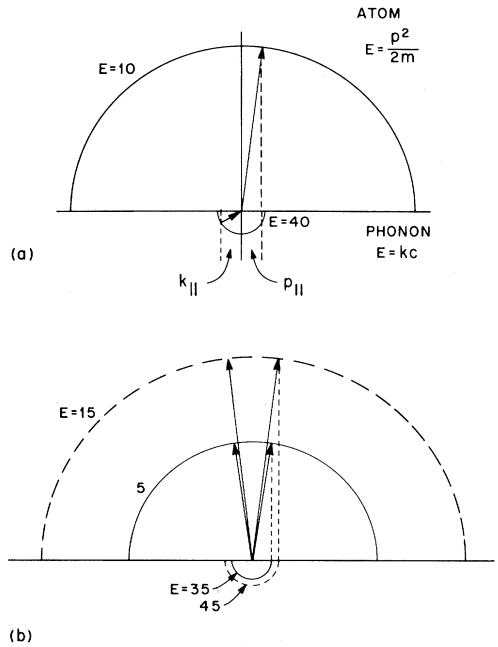

FIG. 15. Curves of constant energy in momentum space for atoms above the interface, and phonons below, drawn to scale with $E_b = 30$ K (all energies in Kelvin). (a) Geometric construction which shows that parallel-momentum conservation leads to atoms emitted almost normal to the interface. (b) The angular width of the atomic critical cone depends on the energy, with the high-energy atoms emitted into a narrower cone. This results in an atomic "rainbow" in the desorption spectrum.

curves of constant energy in momentum space for atoms and phonons, drawn to scale. In order to overcome the binding energy, which we assume to be $E_b = 30k_B$, a phonon with an energy of $40k_B$ is required to produce an atom with $E = 10k_B$. For a given incident phonon, the momentum vector $\vec{p}$ of the desorbed atom can be found by a geometric construction which ensures that $K_{||} = P_{||}$. Figure 15 shows that the atoms are emitted within a cone with half-angle δ given by

$$\delta = \sin^{-1}\left[\frac{E+E_b}{c\sqrt{2mE}}\right], \tag{4.9}$$

which is less than 10° for the example shown. We have used a sound speed of $c = 3\times 10^5$ cm/sec, appropriate for Constantan. Similarly, an energetic atom incident on the surface from a direction outside the cone could not be adsorbed with the emission of a single phonon and would be obliged to reflect specularly from the surface. The similarity with optical total internal reflection suggests the name critical cone.

The kinetic relations imply the existence of another, more subtle, effect in the angular distribution, which is illustrated in Fig. 15(b). Because the atom energy is a quadratic function of momentum while the phonon energy is linear in momentum, the exact value of the critical angle is energy dependent, and low-energy atoms can leave the surface at larger angles than high-energy ones. This correlation between energy and emission angle results in a rainbowlike effect in the desorption signal.

The experimentally observed behavior of the angular dependence of the desorption flux is shown in Fig. 16. The signal intensity is a rapidly decreasing function of angle, reaching half of its normal-incidence value at 15°. In addition, the average arrival time of the atoms increases with increasing angle, or equivalently, the average energy decreases with angle, in accordance with the qualitative results suggested by Fig. 15(b). Quantitatively, however, the observed angular distribution is approximately twice as wide as expected on the basis of the SPCME model. There are several possible explanations for this discrepancy. In the derivation of the SPCME model, we assumed that the parallel momentum of the desorbed atom is due entirely to the parallel momentum of the phonon that desorbed it. In fact, the adatom has some initial parallel momentum which influences the angular distribution. The magnitude of the initial momentum can be estimated in the opposite limits of a strongly localized adsorption site and a completely mobile adsorbate which is at a finite temperature. The momentum which the adsorbed particle acquires by virtue of a transverse localization characterized by a length l is of order $\hbar/l$, which for $l = 2$ Å is equal to the momentum of a free helium atom with $E = 1.4k_B$ or a phonon with $\hbar\omega = 100k_B$. If the adsorbate is modeled as an ideal two-dimensional gas at temperature T, the rms transverse momentum is $(2k_BTm)^{1/2}$, which, for $T = 2$ K, is equal to the momentum of a phonon with $\hbar\omega = 130k_B$. The state of our helium films is probably intermediate between these two extreme cases, but in either model the initial parallel momentum of the adatom is of the same order as the momentum of the desorbing phonon. The effects of the initial adatom momentum can be described phenomenologically by including the atom's parallel momentum $p_{||}$ in the kinematic conservation conditions and introducing a parallel-momentum distribution $g(p_{||})$. The expression for the flux of Eq. (3.2) can be generalized to read

$$J(E,\Omega) = \int\int d^3k\, d^3p_{||} \cos(\theta) g(p_{||}) \frac{f(\omega)}{\omega} \times \delta\left[\hbar\omega + \frac{p_{||}^2}{2m} - E - E_b\right] \times \delta(\vec{K}_{||} + \vec{p}_{||} - \vec{p}\,'_{||}), \tag{4.10}$$

where the inequality

$$E + E_b - p_{||}^2/2m > c[(\vec{p}\,'_{||} - \vec{p}_{||})^2]^{1/2}$$

defines the limits of integration. This integral cannot be conveniently expressed in closed form, but the fact that the region of integration geometrically represents the intersection of a cone and a paraboloid in the atom phase space can be exploited to facilitate the numerical computation of the integral, which can then be used to calculate the expected form of the bolometer signal. Figure 17 shows the results of a calculation of the bolometer signal for the same experimental conditions of Fig. 16, assuming

$$g(p_{||}) \propto \exp(-p_{||}^2/2mk_BT)$$

with T equal to the ambient temperature. The model approximately reproduces both the angular width of the experimental signal and the change in the mean arrival time with angle. The angular width of the signal is quite sensitive to the value of the film temperature as shown in Fig. 18. As the film temperature approaches the substrate temperature, the angular distribution becomes very similar to the $\cos\theta$ distribution expected on the basis of the SDB model.

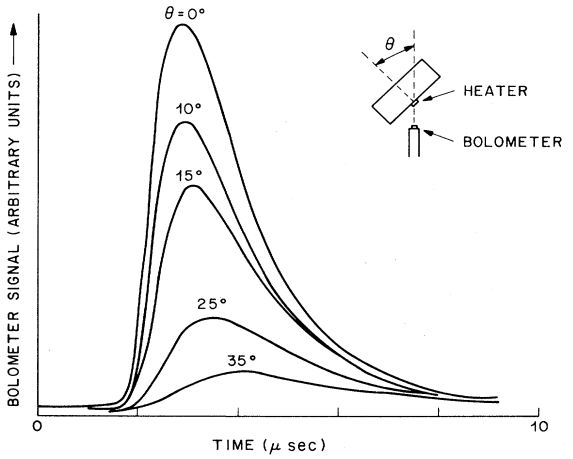

FIG. 16. Experimental bolometer signal as a function of time for several values of θ. $T_h = 8$ K. Experimental geometry is that of Fig. 1(c).

There are a number of alternative possible explanations for the observed angular distribution which do not imply single-particle conservation conditions.[35,36] Of particular

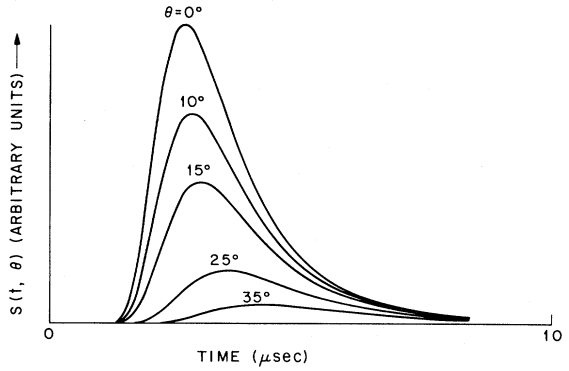

FIG. 17. Computed curves of $S(t,\theta)$ derived from Eq. (4.10) for the same experimental conditions as Fig. 16 except that the initial atomic momentum distribution is similar to an ideal gas at 2 K.

interest is the evidence presented by Cowin *et al.*[35] that collisions among desorbing atoms could produce a focused desorption beam. Although the mechanism of this effect is unclear, computer simulations[37] lend support to this idea. They indicate that on the order of one collision per atom can produce focusing of the desorbed beam without substantially affecting $S(t)$ in the normal direction, in agreement with our observations.

Using the results presented here for the angular distribution, we cannot distinguish between these alternate explanations. However, in the next subsection we present independent evidence for single-phonon desorption, which is not subject to these uncertainties.

D. Phonoatomic effect

In the crystal-substrate geometry, a burst of phonons from the heater, at temperature T_h, spreads out in the crystal before reaching the far surface on which a helium film is adsorbed. For a typical crystal 9.5 mm thick, the phonon intensity at the helium film is reduced by a factor of $\sim 6\times 10^3$ from its value at the heater surface. These

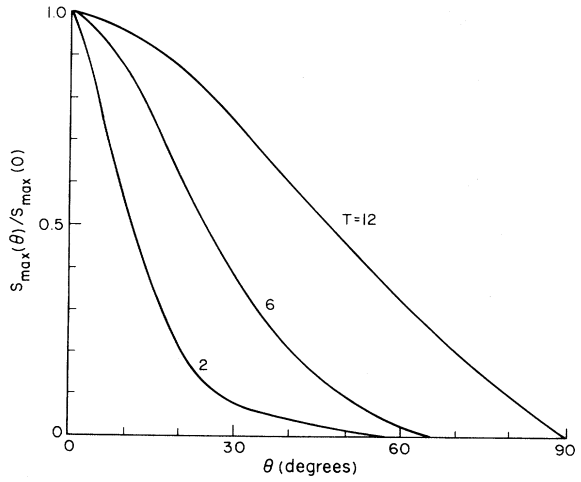

FIG. 18. Angular dependence of the maximum bolometer signal derived from Eq. (4.10) for several values of the film temperature. The phonon temperature is $T_h = 12$ K.

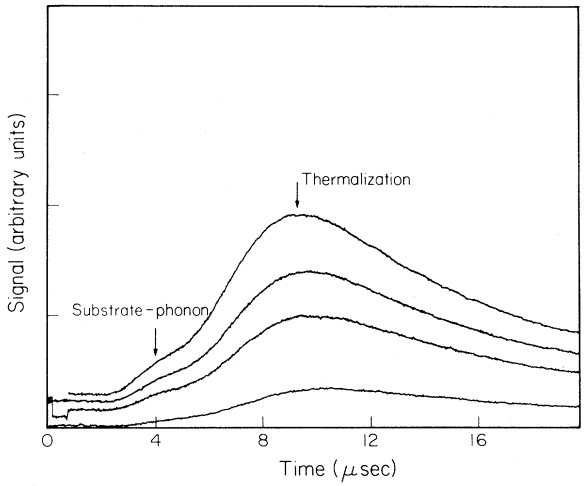

FIG. 19. Bolometer signals versus time for heater powers of 0.23, 0.184, 0.146, and 0.073 W (pulse width 1 μsec). The time scale does not include the photon time of flight (1.72 μsec) in the crystal. Experimental arrangement is that of Fig. 1(b).

phonons cause desorption, which is detected in the usual way. However, in contrast to the experiments described above, the signal in these experiments is enhanced by using a larger source area (the desorption area is delimited by a mask with a circular hole 1 mm in diameter) and by using longer heater pulses (typically ~ 1 μsec).

If the incident phonons are absorbed by the film and thermalized, their intensity is too low to cause appreciable warming of the film. The result then is desorption at slightly above ambient temperature. On the other hand, if hot incident phonons desorb helium atoms directly, these atoms desorb with kinetic energies characteristic of the much higher heater temperature, T_h. These two processes may be distinguished in the resulting signal by their times of flight to the bolometer.

Typical signals[6] are shown in Fig. 19. Both processes, thermal desorption and substrate-phonon desorption, are seen to occur. The large peak is due to thermal desorp-

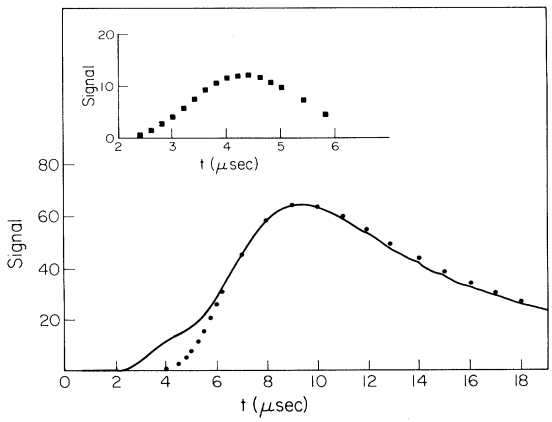

FIG. 20. Fit of the thermal peak to Eq. (3.16) with $n=3$ (solid circles). The inset shows the substrate-phonon peak after subtracting the thermal peak from the measured signal (solid curve).

tion. The shoulder at shorter arrival times is due to direct desorption.

The direct substrate-phonon part of the signal is analogous to a photoelectric effect experiment in that the kinetic energies of the desorbed atoms depend on the frequencies rather than the intensity of the incident-phonon beam. At present, unfortunately, our experiments are constrained to use a thermal, rather than a monochromatic, source of phonons. The incident phonons have a Bose distribution at temperature T_h. Consequently, although only those phonons with energy $\hbar\omega > E_b$ are capable of causing desorption, we have not measured the threshold effect analogous to the work function in photoemission from a metal. Because of the thermal distribution of ω, the result is a Maxwellian distribution of desorbed atoms at temperature T_h, with an amplitude proportional to $\exp(-E_b/k_B T_h)$ [see Eq. (3.2b)].

To analyze data like those in Fig. 19 we have used the SDB model expression, Eq. (3.15). This equation is based on the SDB model for the case of infinity extended source geometry. In the present case, however, t is measured from the time of arrival of the pulse at the desorbing surface. The empirical fit to the thermal peak is shown in Fig. 20. Once this fit is obtained, the thermal peak may be subtracted from the data, leaving the direct phonon peak, also shown in Fig. 20. The area under the direct peak amounts to about 5% of the total signal.

Temperatures are derived from the positions of the peak maxima, t_m, using Eq. (3.16). For both thermal and substrate-phonon peaks, we assumed that $n=3$ in these data. The measured chemical potential ($|\mu| = 22k_B$) is used to evaluate L, as explained in Appendix A. In Table III, heater temperatures computed from Eq. (2.2) are compared to the temperatures of the thermal and single-phonon peaks evaluated by this procedure for the data in Fig. 19. The results confirm our assertion that the thermal peak is due to modest heating above ambient, while the substrate-phonon peak follows the heater temperature.

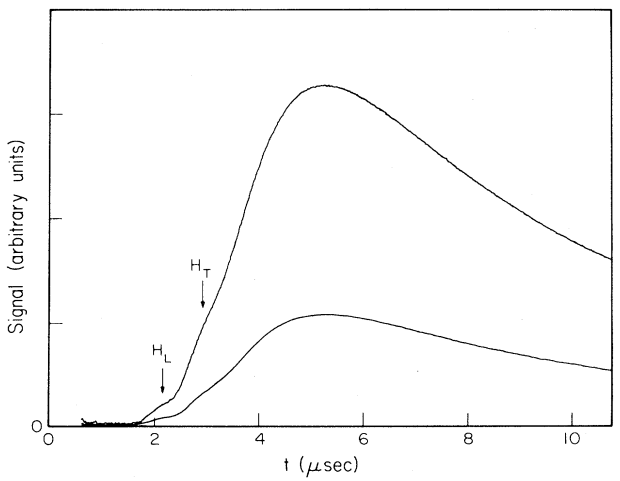

FIG. 21. Bolometer signal, at two different amplifications, when the bolometer is placed very close to the desorbing film, showing desorption of hot atoms by two phonon polarizations ($T_h = 18$ K and pulse width 0.09 μsec). The time scale includes the phonon time of flight through the crystal.

TABLE III. Calculated heater temperatures (T_h) compared to substrate-phonon and thermal desorption temperatures for data shown in Fig. 19.

Heater (acoustic-mismatch theory) T_h (K)	Substrate-phonon peak T_a (K)	Thermal peak T_a (K)
11.1±0.2	10.8±0.4	2.6±0.1
10.5	10.2	2.4
9.9	9.6	2.3

It is also possible to resolve peaks due separately to longitudinal and transverse substrate phonons. To do so, one must use heater pulses which are short compared to the 0.72-μsec difference in the transit time of the two polarizations across a 9.5-mm-thick crystal. In addition, to improve resolution, a smaller mask was used (0.3 mm) and the bolometer was moved closer to the desorbing surface (0.3—0.4 mm). This has the effect of sharpening the Maxwellian distributions for each of the modes of desorption, as well as enhancing the intensity of the signal from a short pulse and narrow aperture.

The result of these manipulations is shown in Fig. 21. The substrate phonon peak may be distinguished as two shoulders, 0.72 μsec apart, denoted H_l and H_T, where the difference in their arrival times and their ratio of intensities agree with those of the longitudinal and transverse phonons at the crystal interface, measured in a separate experiment[4] with a bolometer evaporated directly onto the sapphire surface.

V. SUMMARY AND CONCLUSIONS

The important quantities characterizing the desorption process are the total rate and the velocity distribution as a function of time after the commencement of the heat pulse. These have been measured and the following results have been obtained.

(1) The distribution of v_z is consistent with either of the two simple models discussed in Sec. II—detailed balance and single-phonon constant matrix element.

(2) Because the models and experiments give approximately the same line shape, the desorption signal can be characterized by a temperature. The latter is in good agreement with a calculation of the *heater* temperature based on the Joule heating rate.

(3) The desorption rate is approximately exponential in time. The time constant τ has the Arrhenius form $\tau = \tau_0 \exp(\beta E_0)$, with τ_0 and E_0 values given in Table II and Figs. 11 and 12. Typical results are $\tau_0 \simeq 10^{-9}$ sec and $E_0 \simeq 2|\mu|/3$, where μ is the preexisting equilibrium chemical potential.

(4) The atoms are emitted primarily in the forward direction; approximately one-half emerge within $\theta_m = 20°$ of the normal direction, i.e., a much narrower range than a cosine ($\theta_m = 60°$). The energy distribution varies with θ in a "rainbow" effect.

(5) The alternative to the heater-substrate geometry

used for the experiments above is the crystal-substrate geometry. This experiment allows us to study desorption due to a low-intensity, but high-temperature, phonon flux. In the resulting signal we observe the phonoatomic effect (direct substrate-phonon-induced desorption) as well as conventional thermal desorption.

Our interpretation of these results is guided in part by the simple models of Sec. III. As discussed there, more sophisticated microscopic treatments make detailed assumptions about the interaction with the surface, surface homogeneity, and the absence of mutual interaction between adatoms which seem unwarranted in the present context. Alternatively, the detailed-balance model may be elaborated into what may be called a "thermodynamic model."[32,33] This characterizes the film as a collective entity with an equation of state corresponding to bulk liquid ^{4}He. While not designed for quantitative accuracy, it has been shown to give excellent agreement with some of the present data. For example, the prediction that the temperature of the desorbing atoms becomes equal to that of the heater at very short times is in excellent agreement with the experimental observation (see Fig. 7). The reason is that the thermalization time scale is found to be short compared to the thickness (desorption) time constant τ. In microscopic models the same observation is attributed instead to direct substrate-phonon-induced desorption.

One of the most remarkable results of these experiments is the narrow cone of desorption. At first, the cone might seem difficult to reconcile with the law of detailed balance unless a correspondingly anomalous behavior obtains for the sticking coefficient. This possiblity can be ruled out on the basis of recent experiments[38,39] which indicate that the sticking coefficient is ~ 0.8, even at incident angles as large as 45°. An alternative possibility is that the regime of these experiments is far from equilibrium. The discussion in Secs. III and IV makes it clear that many phonons are required to equilibrate the motion along the surface. In the presence of a high-intensity, high-frequency phonon flux, the atoms will desorb prior to this equilibration. Thus, the observed cone may be evidence for lateral nonequilibration. It is also possible that the cone is a consequence of collisions among desorbing atoms.

The phonoatomic effect experiment yields another intriguing result which has a plausible interpretation. We attribute the shoulder at the leading edge to direct desorption by high-frequency incident phonons and the large peak to thermal desorption following the absorption of lower-frequency phonon energy in the surface region. The high phonon intensities which keep the film far from equilibrium in the heater-substrate geometry are absent in this case, so we do not expect the thermal peak to have a forward cone. Thus, an interesting test of these ideas is to look for the angular dependence of desorption in the crystal-substrate geometry. The prediction we make is that the phonoatomic bump observed at normal emission (Fig. 19) would be absent at angles $\theta \gtrsim 20°$.

One of the mysteries in these results is the linear relation between the activation energy E_0 and the ambient chemical potential. The thermodynamic model has $E_0 = |\mu|$, but the observed value is two-thirds of this. Naively, one might have expected instead a *larger* value because the equilibrium $|\mu|$ is smaller than the instantaneous value as the film depletes. We have no explanation to offer of this simple, but mysterious, observation.

In this study we have found that careful examination of certain aspects of desorption (line shape, time constant) yields important new insights, but cannot distinguish between radically different models of desorption. However, we have also demonstrated new techniques (angular distribution, phonoatomic effect, the differential technique) that do give promise of leading to deeper understanding as the study of desorption is pursued to new regimes of temperature, coverage, and incident-phonon intensity.

ACKNOWLEDGMENTS

This research was supported in part by the U. S. Office of Naval Research under Contract No. N0014-80-C-0447 and by the National Science Foundation under Grant No. DMR-81-13262. Part of it was completed while one of us (M.W.C.) was a guest at the Institute for Theoretical Physics at the University of California (Santa Barbara). The hospitality of that Institution is gratefully acknowledged.

APPENDIX A: EFFECTIVE LATENT HEAT OF THE FILM, L

Since the bolometer signals in these experiments change slowly compared to the intrinsic bolometer time constant [$\lesssim 50$ nsec (Refs. 3 and 4)], we may regard the deposition of atoms on the bolometer as steady state and isothermal, the flux of energy $\langle \alpha E_d \rangle \dot{N}_0$ maintaining the bolometer temperature at T, above the ambient T_0; Eq. (3.5) may be interpreted to mean

$$S_0 \sim (T - T_0) \sim \langle \alpha E_d \rangle \dot{N}_0 \ . \tag{A1}$$

This flux of heat into the bolometer is removed from the film-gas system whose total energy is $U_f + U_g$, and is written

$$\begin{aligned} \langle \alpha E_d \rangle \dot{N}_0 &= -\frac{\partial}{\partial t}(U_f + U_g) \\ &= -\left[\left[\frac{\partial U_f}{\partial N} \right]_T + \frac{dU_g}{dN} \right] \alpha \dot{N}_0 \ . \end{aligned} \tag{A2}$$

The energy of the gas changes by the kinetic energy of the atom deposited,

$$\frac{dU_g}{dN} = -E \ , \tag{A3}$$

and the change in energy of the film is evaluated assuming the film is, at all times, in internal thermodynamic equilibrium,

$$\frac{\partial U_f}{\partial N} = T \left[\frac{\partial S_f}{\partial N} \right]_T + \mu \ , \tag{A4}$$

where S_f is the entropy of the film and N is the number of atoms in the film. The chemical potential of the film

is equal to that of a hypothetical gas in equilibrium with it, μ_{g0}, which obeys

$$\mu_{g0}=\frac{U_{g0}-TS_{g0}+PV_{g0}}{N_{g0}}=\frac{3}{2\beta}-T\frac{S_{g0}}{N_{g0}}+\frac{1}{\beta}\ . \quad \text{(A5)}$$

Thus we take E_d to be

$$E_d=E-5/2\beta+q_{\rm st}\ , \quad \text{(A6)}$$

where

$$q_{\rm st}=T\left[\frac{S_{g0}}{N_{g0}}-\left[\frac{\partial S_f}{\partial N}\right]_T\right]. \quad \text{(A7)}$$

The quantity $L\equiv q_{\rm st}-5/2\beta$ which is needed to evaluate, e.g., Eq. (4.2), is obtained, in practice, from the chemical potential of the film, measured independently as explained in Sec. II. Using Eqs. (A7) and (A5), we find

$$L=-\mu-T\left[\frac{\partial S_f}{\partial N}\right]_T. \quad \text{(A8)}$$

Here $T(\partial S_f/\partial N)_T$ is typically a small correction ($<\sim 10\%$) to $-\mu$ at the temperature of the bolometer. Since $(\partial S_f/\partial N)_T$ for the bolometer is not accurately known, the specific entropy of bulk liquid helium at the same temperature is used instead.

APPENDIX B: SPECIFIC GEOMETRIES

Here we fill in the details of the calculations reported in Sec. III for three different geometrical cases.

1. Very-small-area source

We treated the case where the desorbing area $A_s \ll l^2$, so that it can be treated as a pointlike origin for the particle trajectories. We take the bolometer to be circular, centered about the intersection of the surface normal with the bolometer plane. The rim of the circle lies at polar angle θ_m relative to this axis. Then particles emitted at $t=0$ will arrive at the detector at time $t=l/v_z$ only if their parallel velocities are less than $v_z\tan\theta_m$. Thus the integrals in (3.10) and (3.12) have this upper limit of integration for $(v_x^2+v_y^2)^{1/2}$. Performing the integration, we obtain

$$I_N=(2\pi A_s/m\beta)(1-e^{-X_m})\ , \quad \text{(B1)}$$

$$I_S=(2\pi A_s/m\beta)[(1-e^{-X_m})(E_z+L+\beta^{-1}) -(X_m/\beta)e^{-X_m}]\ , \quad \text{(B2)}$$

$$X_m\equiv\beta E_z\tan^2\theta_m=\beta_m l^2\tan^2\theta_m/2t^2\ . \quad \text{(B3)}$$

In the opposite limits of very small or infinite detector size, the signal (3.11) satisfies

$$e^{\beta E_z}S_0(t,0)\sim\begin{cases}(L+E_z+\beta^{-1})t^{-3} & \text{(large detector)}\ , \quad \text{(B4a)}\\ (L+E_z)t^{-5} & \text{(small detector)}\cdot \quad \text{(B4b)}\end{cases}$$

The difference in energy prefactor arises from the fact that β^{-1} is the average contribution per particle from its parallel kinetic energy. This is negligible for a point detector, so only E_z enters.

Equations (B4) can be written in reduced form, which permits a line-shape analysis of the parameters (especially the film temperature). This is discussed in Sec. III D.

2. Finite-area source and detector

We shall address briefly the cases of small, but finite, area detector and either small or infinite source. Assume both to be squares with sides $2b$ (source) and $2a$ (detector), respectively. Consider particles emitted a given point $\vec{\rho}=(X,Y)$ which pass through the detector plane ($z=l$) at $\vec{\rho}=(X',Y')$. Those having $|X'|$ and $|Y'|\le a$ will strike the detector. Then, the X component of velocity must satisfy

$$v_1\equiv -u(1+x)<v_x<u(1-x)\equiv v_2\ , \quad \text{(B5)}$$

$$u=av_z/l,\quad x=X/a\ . \quad \text{(B6)}$$

In evaluating the integral over v_x in Eq. (3.10), we integrate only over this interval. For small u, the relevant integral is

$$I_x=\int_{v_1}^{v_2}dv_x e^{-\beta E_x}\equiv I_0+\delta I\ , \quad \text{(B7)}$$

$$I_0=\int_{-u}^{u}dv_x e^{-\beta E_x}\simeq 2u(1-\epsilon/3)\ , \quad \text{(B8)}$$

$$\epsilon=m\beta u^2/2\ , \quad \text{(B9)}$$

$$\delta I/u=\left[\int_{-(1+x)}^{-1}dz-\int_{1-x}^{1}dz\right]e^{-\epsilon z^2} =e^{-\epsilon}\int_0^x dz\, e^{-\epsilon z^2}(e^{-2\epsilon z}-e^{2\epsilon z})\ ,$$

$$\delta I\simeq -2\epsilon x^2 e^{-\epsilon}\ . \quad \text{(B10)}$$

$$I_x\simeq 2u(1-\epsilon/3-\epsilon x^2 e^{-\epsilon})\ . \quad \text{(B11)}$$

The approximations in (B8) and (B10) require ϵ and $\epsilon x\ll 1$. Since a typical v_z is of order $(m\beta)^{1/2}$, this means $a\ll l$ and $aX\ll l^2$. Thus (B11) places restrictions on the sizes of both source and detector. An identical procedure for the y coordinate is straightforward, giving $I_N=I_xI_y$ as

$$I_N=(A_s+a^2v_z^2/l^2)\left[1-\frac{\beta m v_z^2}{2l^2}\left[\frac{2a^2}{3}+\frac{A_s}{2\pi}\right]\right], \quad \text{(B12)}$$

where the term in large square brackets must be small for the approximation to be valid. Thus we may write it as an expansion of an exponential. Since this term multiplies $\exp(-\beta m l^2/2t^2)$ in Eq. (3.9), the effect of finite geometries is equivalent to replacing l in the Boltzmann factor by an effective length $l_{\rm eff}$ defined by

$$l_{\rm eff}^2=l^2+2a^2/3+A_s/2\pi\ . \quad \text{(B13)}$$

This has a simple interpretation as a weighted mean-square distance. Particles arriving at the given time t travel a longer distance than in the case discussed in subsection 1 above, so their probability is reduced appropriately.

We next address the opposite limit of a source of infinite extent compared to the detector ($b\gg a$). As above, we may consider X and Y integrals independently. The

former is

$$\int_{-b}^{b} dX \int_{v_1}^{v_2} dv_x \exp(-\beta E_x)$$
$$= au \int_{-b/a}^{b/a} dx \int_{-x-1}^{-x+1} dz\, e^{-\epsilon z^2}$$
$$= 2au \int_{-\infty}^{\infty} dz\, e^{\epsilon z^2} = 2au(\pi/\epsilon)^{1/2} , \quad \text{(B14)}$$

since $B \gg a$. Thus $I_N = 8\pi a^2/\beta m$. Similarly, one finds $I_S = (E_a + L + \beta^{-1}) I_N$, yielding, in this case of infinite ratio of source to detector size,

$$S_0(t,0) = K v_z^S \alpha^2(v_z) e^{-\beta E_z} (8m\beta/\pi)^{1/2} a^2 (L + E_z + \beta^{-1})/l . \quad \text{(B15)}$$

Comparing this with Eqs. (B4), we note that the same t^{-3} prefactor occurs in the opposite limiting case of a point source and infinite detector.

3. One-dimensional source

Here we analyze the geometry reported by Cohen and King.[1] We take the detector to be a small square with sides of length $2a$. The wire is represented by a flat strip along the X axis, having a very small width δY and length $2b$. Thus Eq. (3.10) becomes

$$I_N = (2av_z/l)^2 \delta Y \int_{-b}^{b} dX \exp(-\beta m X^2 v_z^2/2l^2)$$
$$\sim v_z \mathrm{erf}(b v_z/v_t l) , \quad \text{(B16)}$$

where we have omitted prefactors and defined a typical thermal velocity

$$v_t = (2/\beta m)^{1/2} . \quad \text{(B17)}$$

The sensitivity of the field-ionization detector is reported[1] to be inversely proportional to velocity. Thus in deriving the signal the integral (B16) should be divided by v_z times the average secant of incident angles. The latter geometrical factor will be omitted here for simplicity; no qualitative conclusion is altered. Incorporating v_z^2 in the above, we obtain, from (3.5),

$$S \sim v_z^S a(v_z) \mathrm{erf}(b v_z/v_t l) \exp(-\beta E_z) . \quad \text{(B18)}$$

The line shapes of Cohen and King are consistent with $\alpha(v_z)$ being inversely proportional to v_z (for values of order v_t). *Assuming* this dependence, increasing b beyond $b = 1$ does not change the short-time part of the curve. This is because of the constraint $v_z = v_z X/l$; the associated energy for $X \gtrsim l$ becomes excessive if $v_x \gtrsim v_t$, so the ends of the wire do not contribute. For most relevant times ($t \sim t_t = l/v_t$), the error function can be expanded, yielding

$$S \sim t^{-3} \exp[-t_t^2 (l + b^2/3l^2)/t^2] . \quad \text{(B19)}$$

The peak shifts with b as

$$t_m = t_t (1 + b^2/3l^2)^{1/2} , \quad \text{(B20)}$$

which is equivalent to replacing l by $(l^2 + b^2/3)^{1/2}$.

[1] S. A. Cohen and J. G. King, Phys. Rev. Lett. **31**, 703 (1973); K. Andres, R. C. Dynes, and V. Narayanamurti, Phys. Rev. A **8**, 2501 (1973).

[2] J. Eckardt, D. O. Edwards, F. M. Gasparini, and S. Y. Shen, in *Low Temperature Physics LT-13,* edited by K. D. Timmerhaus, W. J. O'Sullivan, and E. F. Hammell (Plenum, New York, 1974), Vol. 1, p. 518; D. O. Edwards, G. G. Ihas, and C. P. Tam, Phys. Rev. B **16**, 3122 (1977).

[3] P. Taborek, M. Sinvani, M. Weimer, and D. Goodstein, J. Phys. (Paris) Colloq. **6**, 825 (1981).

[4] P. Taborek, M. Sinvani, M. Weimer, and D. Goodstein, J. Phys. (Paris) Colloq. **6**, 852 (1981); **6**, 855 (1981).

[5] M. Sinvani, P. Taborke, and D. Goodstein, Phys. Rev. Lett. **48**, 1259 (1982).

[6] M. Sinvani, P. Taborek, and D. Goodstein, Phys. Rev. Lett. **95A**, 59 (1983).

[7] P. Taborek, Phys. Rev. Lett. **48**, 1737 (1982).

[8] M. Sinvani and D. Goodstein, Surf. Sci. **125**, 291 (1983).

[9] P. Taborek and D. L. Goodstein, J. Phys. C **12**, 4737 (1979).

[10] P. Taborek and D. L. Goodstein, Phys. Rev. B **22**, 1550 (1980).

[11] P. Herth and O. Weis, Z. Agnew, Phys. **29**, 101 (1970).

[12] O. Weis, J. Phys. (Paris) Colloq. **33**, C4-48 (1972).

[13] P. Taborek and D. Goodstein, Rev. Sci. Instrum. **50**, 227 (1979). Grafoil manometry was dependable when $-\mu < 30$ Kelvin.

[14] W. H. Keesom, *Helium* (Elsevier, Amsterdam, 1942).

[15] R. L. Elgin and D. Goodstein, Phys. Rev. A **9**, 1657 (1974).

[16] M. Bienfait, J. G. Dash, and J. Stoltenberg, Phys. Rev. B **21**, 1765 (1980).

[17] The coefficient of the z^{-3} van der Waals adsorption potential is exceptionally large for graphite. See G. Vidali and M. W. Cole, Surf. Sci. **110**, 10 (1981).

[18] J. E. Lennard-Jones and C. Strachan, Proc. R. Soc. London, Ser. A **150**, 442 (1935).

[19] A review is presented by M. W. Cole and F. Toigo, in *Interfacial Aspects of Phase Transformations,* edited by B. Mutaftschiev (Reidel, Dordrecht, The Netherlands, 1982), p. 223.

[20] F. O. Goodman, Surf. Sci. **24**, 667 (1971).

[21] B. Bendow and S. C. Ying, Phys. Rev. B **7**, 622 (1973).

[22] S. C. Ying and B. Bendow, Phys. Rev. B **7**, 637 (1973).

[23] F. O. Goodman and I. Romero, J. Chem. Phys. **69**, 1086 (1978).

[24] Z. W. Gortel, H. J. Kreuzer, and D. Spaner, J. Chem. Phys. **72**, 234 (1980).

[25] Z. W. Gortel, H. J. Kreuzer, and R. Teshima, Phys. Rev. B **22**, 5655 (1980).

[26] Z. W. Gortel, H. J. Kreuzer, and R. Teshima, Phys. Rev. B **22**, 512 (1980).

[27] P. Summerside, E. Sommer, R. Teshima, and H. J. Kreuzer, Phys. Rev. B **25**, 6235 (1981).

[28] F. O. Goodman, Surf. Sci. **120**, 251 (1982).

[29] E. Sommer and H. J. Kreuzer, Phys. Rev. Lett. **49**, 61 (1982). This reference treats adatom interactions in a mean-field approximation.

[30] C. Jedrzejk, K. F. Freed, S. Efrima, and H. Metiu, Chem. Phys. Lett. **79**, 227 (1981).

[31] M. W. Cole and F. Toigo, Surf. Sci. **119**, L346 (1982).

[32] D. L. Goodstein and M. Weimer, Surf. Sci. **125**, 227 (1983).

[33] M. Weimer and D. Goodstein, Phys. Rev. Lett. **50**, 193 (1983).

[34]M. K. Maul and M. W. P. Strandberg, J. Appl. Phys. **40**, 2822 (1963).
[35]J. P. Cowin, D. J. Auerbach, C. Becker, and L. Wharton, Surf. Sci. **78**, 545 (1978).
[36]F. O. Goodman [Phys. Rev. B **27**, 6478 (1983)] provides an alternate explanation for these effects which does not rely on single-particle conservation conditions.
[37]P. Taborek (unpublished).
[38]M. Sinvani, M. W. Cole, and D. L. Goodstein, Phys. Rev. Lett. **51**, 188 (1983).
[39]M. Sinvani, D. L. Goodstein, and M. W. Cole, Phys. Rev. B **29**, 3905 (1984).

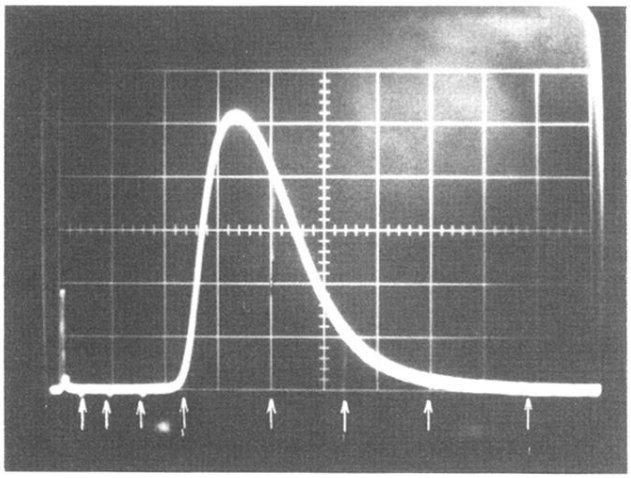

FIG. 8. Desorption signal for different values of pulse width $0.2 < t_p < 9$ μsec. The arrows indicate the ends of the pulses. Shown are eight saturated signals for different pulse widths, exposed on the same camera film.